

BIOMATERIALS

Deformable hard tissue with high fatigue resistance in the hinge of bivalve *Cristaria plicata*

Xiang-Sen Meng^{1†}, Li-Chuan Zhou^{2,3†}, Lei Liu^{1†}, Yin-Bo Zhu², Yu-Feng Meng¹, Dong-Chang Zheng², Bo Yang¹, Qi-Zhi Rao⁴, Li-Bo Mao^{1*}, Heng-An Wu^{2*}, Shu-Hong Yu^{1,5*}

The hinge of bivalve shells can sustain hundreds of thousands of repeating opening-and-closing valve motions throughout their lifetime. We studied the hierarchical design of the mineralized tissue in the hinge of the bivalve *Cristaria plicata*, which endows the tissue with deformability and fatigue resistance and consequently underlies the repeating motion capability. This folding fan-shaped tissue consists of radially aligned, brittle aragonite nanowires embedded in a resilient matrix and can translate external radial loads to circumferential deformation. The hard-soft complex microstructure can suppress stress concentration within the tissue. Coherent nanotwin boundaries along the longitudinal direction of the nanowires increase their resistance to bending fracture. The unusual biomineral, which exploits the inherent properties of each component through multiscale structural design, provides insights into the evolution of antifatigue structural materials.

Brittle materials are extensively used as structural or functional components in various fields such as aerospace, tissue engineering, and electronics (1–3). However, artificial brittle materials are sensitive to microcracks and imperceptible defects and thus suffer from the risk of cumulative fatigue damage caused by the prolonged cyclic loading, which can eventually cause catastrophic failure (4–7). In this respect, living organisms produce rigid biominerals such as nacre (8), bone (9), and tooth (10) in which the fatigue tolerance is greatly improved but the native high strength and rigidity of the minerals are retained. The fatigue damage in these biominerals, such as crack propagation, can be shielded by extrinsic mechanisms, including crack bridging, deflection, and branching (8–11).

Although these biominerals have inspired fatigue-tolerant artificial materials such as tough biomimetic ceramics (12, 13), more and diverse design principles have to be uncovered to extend the scope of artificial materials. For example, materials with high flexibility have received intense focus owing to the development of foldable and wearable devices (14, 15). Existing antifatigue models derived from very

rigid biominerals such as nacre are not effective for the design of such flexible materials. Besides the lack of flexibility, the fatigue tolerance of these models strongly relies on the rising R-curve behavior during crack propagation (11), yet the crack extension can cause irreversible impacts on the device performances (16, 17). This indicates that the protection of the brittle components in such devices against fatigue should not be overdependent on the mechanisms that only come into effect in the crack wake (2, 11).

Macrostructures and mechanical performance

We report the antifatigue design of the deformable calcareous tissue in the hinge of the bivalve shell *Cristaria plicata* (Fig. 1A, i, and fig. S1A) (18). This tissue exhibits both high deformability and exceptional fatigue resistance during the hundreds of thousands of repeating opening-and-closing (ROAC) motions of the shell valves. The hinge is located at the dorsal edge of the bivalve shell, by which the two valves are joined together, and functions as the axis of the ROAC motions (Fig. 1, A, ii, and B, i; fig. S1; and movie S1) (19). It undergoes large deformation during the closing process of two rigid valves driven by the adductor muscles and provides the driving force for the spontaneous valve opening by releasing the stored elastic potential energy (movie S2) (20).

To verify the mechanical and antifatigue performance of the hinge, we performed cyclic loading tests that simulated the ROAC motions on freshly prepared *C. plicata* samples (fig. S2A and movie S3) (21). No obvious fatigue failure was observed even after 1,500,000 cycles under natural working conditions (Fig. 1C and figs. S3 and S4A). We also imposed a larger load (about 20% overload) on the edge-trimmed samples (fig. S2), and the hinge exhibited similar behavior in this case (Fig. 1C and figs. S4B and S5). To investigate the antifatigue per-

formance of the hinge under much larger loads, we further increased the load stepwise to about 100% overload in the cyclic tests (fig. S6). Its function is still largely preserved, although the resilience of the hinge decreases under such conditions.

Reconstructed x-ray microcomputed tomographic (μ CT) images reveal the inhomogeneous electron density distribution in the hinge, which is surrounded by a porous tissue and two slab areas (Fig. 1B, ii, and fig. S1F). Given the differences in both optical and μ CT images (Fig. 1B), the hinge area can be divided into two distinct regions: a folding fan-shaped region (FFR) and an outer ligament (OL). Elemental mapping images reveal a sharp increase of calcium concentration from the OL to the FFR (Fig. 1D), which is consistent with the elastic modulus and hardness variations of the regions in the dried hinge and the density difference in the μ CT image (Fig. 1E and fig. S7) (22). This correlation can be explained by calcium carbonate in the form of aragonite being the only mineral phase in the two hinge regions that can be observed with powder x-ray diffraction (fig. S8) (23).

We monitored the two hinge regions to unravel their roles during the ROAC motions (Fig. 2A and movie S4). During closing, the FFR region is pushed by the rotating slab areas that are bound to the valves. The two sides of the FFR then rotate, and the whole FFR region simultaneously bends and deforms in the circumferential direction, which is accompanied with the stretch of the OL (Fig. 2A). The FFR undertakes a minor radial deformation and provides robust radial support to fix the OL to ensure effective OL circumferential stretch. We validated this behavior by means of finite element analysis (FEA) during the closing process (Fig. 2B, fig. S9, and movie S5), and the behavior reverses during opening. Therefore, the structure of the FFR, which is similar to that of traditional arch structures, can effectively translate the external radial load to the circumferential deformation. We also calculated the stress distributions in the FEA model along both circumferential and radial directions at the open and closed states, respectively (Fig. 2, C to E, and supplementary text 1). The circumferential tensile stress in the hinge is mainly borne by the OL (Fig. 2D and fig. S10), which agrees with the measured result that the stress along the circumferential direction is much higher in the OL than that in the FFR (Fig. 2, F and G, and fig. S10).

In addition, given that the OL and the outermost edge of the FFR are bound together, the deformations are supposed to be similar for both when stretched. The elastic strain energy released by the FFR and the OL was derived by integrating the products of the energy density of each element by its volume

¹Department of Chemistry, Institute of Biomimetic Materials and Chemistry, Anhui Engineering Laboratory of Biomimetic Materials, New Cornerstone Science Laboratory, Division of Nanomaterials and Chemistry, Hefei National Research Center for Physical Sciences at the Microscale, University of Science and Technology of China, Hefei 230026, China.

²CAS Key Laboratory of Mechanical Behavior and Design of Materials, Department of Modern Mechanics, CAS Center for Excellence in Complex System Mechanics, University of Science and Technology of China, Hefei 230027, China.

³School of Mechanical Engineering, Hefei University of Technology, Hefei 230009, China. ⁴Anhui Shuyan Intelligent Technologies Co., Wuhu 241200, China. ⁵Institute of Innovative Materials, Department of Materials Science and Engineering, Department of Chemistry, Southern University of Science and Technology, Shenzhen 518055, China.

*Corresponding author. Email: maolb@ustc.edu.cn (L.-B.M.); wuha@ustc.edu.cn (H.-A.W.); shuyu@ustc.edu.cn (S.-H.Y.)

†These authors contributed equally to this work.

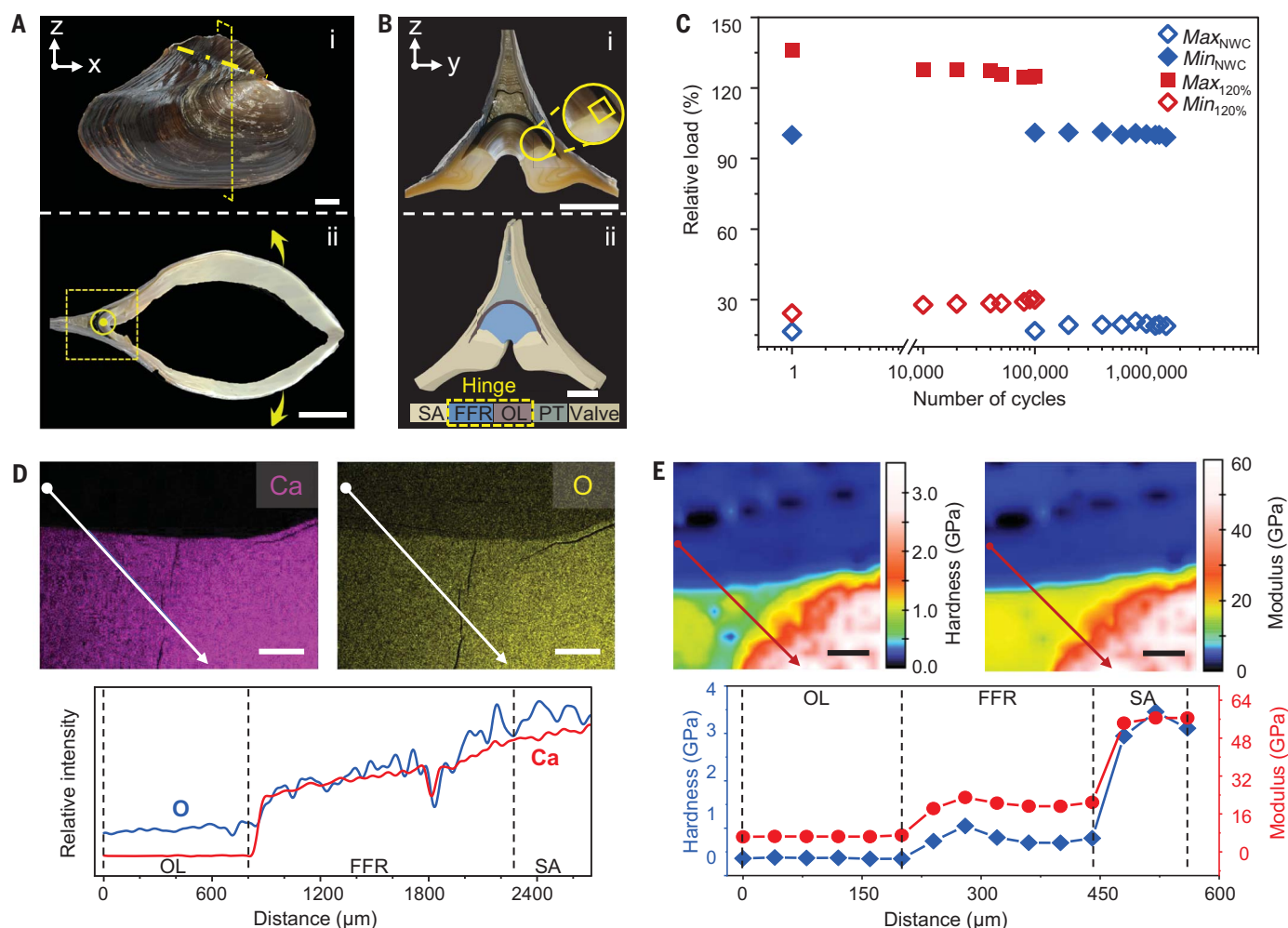


Fig. 1. Structural features and mechanical properties of the hinge. (A) (i) Optical image of *C. plicata* and (ii) sectional photograph of the shell at the cutting plane (dotted rectangle) shown in (i). The yellow dash-dotted line in (i) represents the hinge axis as well as the axis of the ROAC motions. This axis is indicated with the circled dot in (ii). Scale bars, 2 cm. (B) (i) Optical image and (ii) reconstructed three-dimensional μ CT image of a polished hinge sample viewed in the longitudinal direction [(A), ii, dashed box]. The different colors in (ii) indicate the distinct regions in the hinge: FFR, blue; OL, saddle brown; slab areas (SAs), sienna; porous tissue (PT), light cyan; and valve, pale yellow. The SAs exhibit a slightly

lighter gray color than that of the nacreous part of the valves, indicating a higher electron density. Scale bars, 1 cm. (C) Relative maximum and minimum loads in the fatigue tests under the natural working condition (NWC) and overloading condition (about 20% overload) (supplementary materials, materials and methods). (D) Elemental maps and line scans showing the calcium (Ca) and the oxygen (O) distributions in the yellow square in (B), in which the FFR, the OL, and the SAs are included. Scale bars, 500 μ m. (E) Maps of the elastic modulus and hardness of the yellow square in (B) and the corresponding line scans from the OL to the FFR and then the SA of a dried sample. Scale bars, 200 μ m.

in the numerical model. The results suggest that the OL stores most of the elastic strain energy during closing, which is then released to sustain valve opening (supplementary text 1 and fig. S11). Compressive tests show that the FFR is highly anisotropic (Fig. 2, G and H). In the radial direction, the whole FFR is under compressive stress (Fig. 2E), which is associated with the radial support of the FFR to the OL. Nevertheless, the deformation of the FFR in this direction is limited by the space of the entire hinge area (Fig. 2, A and B). Compensatorily, the FFR has a much larger tangent modulus along the radial direction compared with that along the circumferential direction (Fig. 2, G and H). Therefore, it can translate sufficient radial load to support the OL within

a very small radial deformation. By contrast, the FFR can deform much easier circumferentially, which allows the FFR to adapt itself to the hinge deformation. These observations reveal that as a dense and relatively rigid calcareous tissue (figs. S8 and S12 and tables S1 and S2), the FFR endures a large radial load to support the OL while undertaking a large circumferential deformation during the ROAC motions of the valves without fatigue failure (more than 1,500,000 cycles). This distinguishes the FFR from other biominerals such as nacre, cortical bone, and human enamel (table S3). Once produced, the acellular FFR begins to function during the ROAC motions. Yet it neither comes in contact with cells, like the nacreous inner layer of the valves does, nor contains any

cells inside and thus cannot be repaired after being damaged, suggesting that the FFR has to be inherently robust (fig. S13) (24, 25).

Microstructures and crystallographic features

To understand the mechanisms of the mechanical function and antifatigue performance of the FFR, we analyzed its microstructures and crystallographic features. The fracture surface of the FFR exhibits a concentrically laminated structure (Fig. 1B, i, and fig. S14). Each layer consists of tightly aligned and stacked, long nanowires with diameters of about 100 to 200 nm (Fig. 3A). Detailed measurements reveal that the diameters increase gradually from the inner part of one nanowire layer to the outer part (fig. S15). Such laminated structure

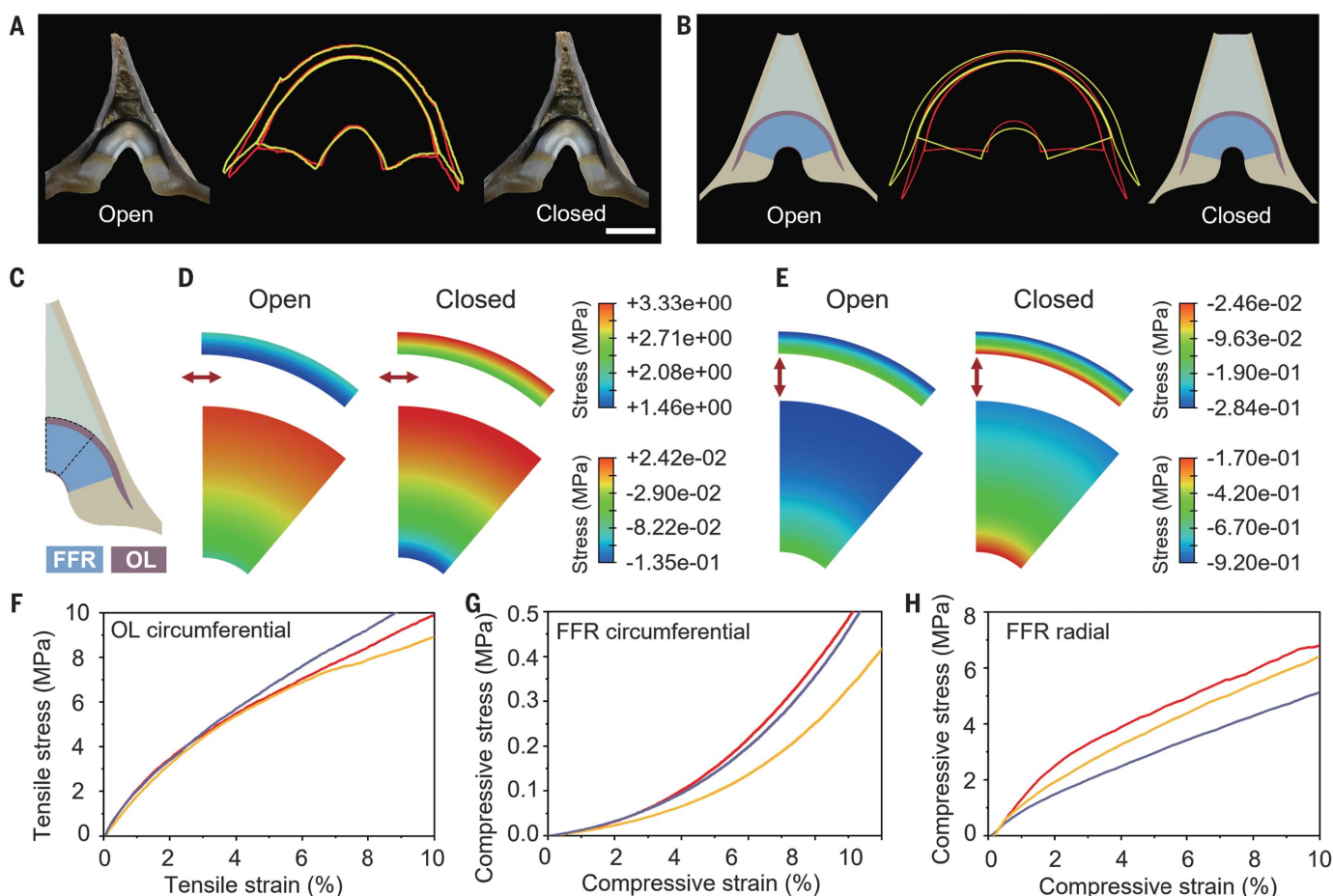


Fig. 2. Transmission relationship of the ROAC motions. (A) Optical images and (B) FEA models of the hinge in an open state and a closed state. The contours of the FFR and the OL at the two states are compared. Yellow, open state; red, closed state. Scale bar, 500 μm . (C to E) FEA of the stress distributions in (C) the hinge

along (D) the circumferential and (E) radial directions. The red arrows indicate the directions of the stresses. (F) Tensile tests of the OL and (G and H) compressive tests of the FFR (freshly prepared wet sample) along the (G) circumferential and (H) radial directions, showing the different mechanical performances of these regions.

and varying nanowire diameters can help the FFR accommodate the nanowire space-filling pattern.

Additionally, the cross section of each nanowire exhibits a pseudo-hexagonal shape (Fig. 3B) (26). We decalcified an FFR sample with an ethylenediaminetetraacetic acid disodium salt dihydrate solution to remove the aragonite minerals (27). The remnant shows a typical honeycomb-like structure, indicating that the aragonite nanowires are embedded in a continuous organic matrix (Fig. 3, C and D; fig. S12; and table S2). The nanowire orientations at several sampling positions in the fracture surface of the FFR suggest that they are radially oriented in the whole region, which are similar to the ribs in a folding fan (Fig. 3I and fig. S16). Micro x-ray diffraction mapping of the same surface reveals that the aragonite nanowires uniformly grow along the $\langle 002 \rangle$ crystallographic direction (Fig. 3J) (28), which agrees with the high-resolution transmission electron microscopy (HRTEM) analysis (Fig. 3, E to H). These results indicate that the mor-

phological and the $\langle 002 \rangle$ crystallographic orientations of the aragonite nanowires match each other. This preferred $\langle 002 \rangle$ growth orientation of the nanowires is also the fastest growth direction during abiotic aragonite crystallization (29, 30). Although biological control can substantially change the mineralization process, the crystallographic anisotropy in growth rate can contribute to the biominerals formation with highly anisotropic morphologies, leading to a more cost-effective biomineralization process (31, 32).

Origins of deformability and fatigue resistance

To study the role of the morphological and crystallographic orientations of the aragonite nanowires in functionality, we extracted a representative volume element (RVE) from the FFR and simulated its response to loads along different directions (fig. S17). In the direction that is normal to the nanowires, which is the circumferential direction in the FFR, the RVE can easily deform because of its relatively low modulus (fig. S17, A and C). In the direction

that is parallel to the nanowires, which is the radial direction in the FFR, the RVE can transfer a large load with a limited deformation (fig. S17, B and D). We also found that the RVE with aragonite nanowires uniformly oriented in the $\langle 002 \rangle$ direction exhibits a higher stress level than that oriented in the $\langle 100 \rangle / \langle 010 \rangle$ at the same strain (fig. S17D), indicating that the former can transfer larger radial loads. Given that the $\langle 002 \rangle$ crystallographic direction has the fastest growth rate during the aragonite crystallization (30), the above analyses suggest an elegant consistency of the mechanically favored orientation, the thermodynamically favored orientation, and the actual nanowire crystal growth direction. Consequently, although the FFR is fabricated in a cost-effective way concerning the nanowire growth direction, the microstructures and crystallographic features of the FFR are also optimized for the sake of good circumferential deformability and radial load translation capability, both of which are the cornerstones of the long-term functioning performance of the FFR (Fig. 2).

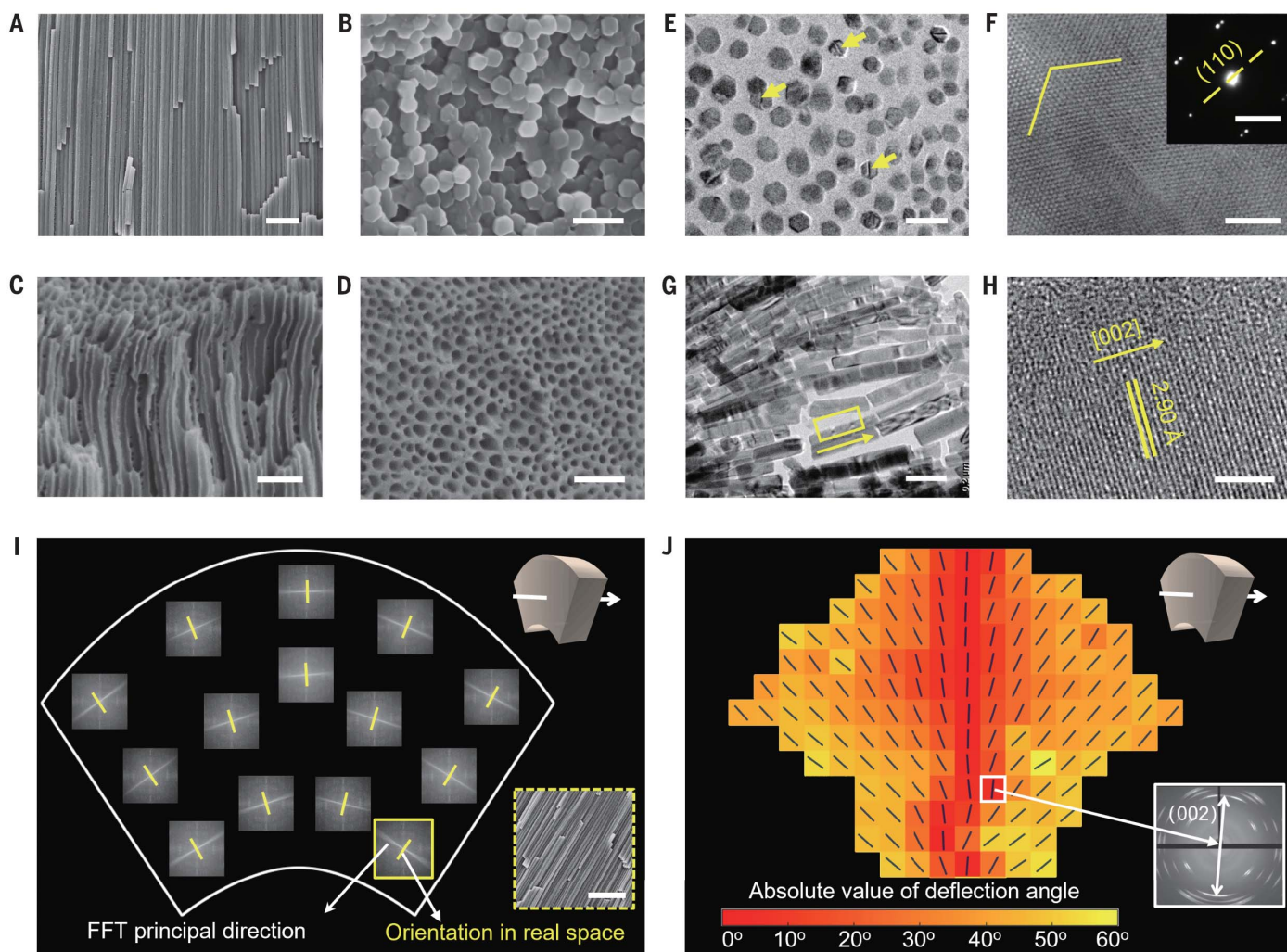


Fig. 3. Microstructural and crystallographic features of the aragonite nanowires in the FFR. (A) Longitudinal and (B) cross-sectional fracture surfaces of the FFR showing the oriented nanowires with a pseudo-hexagonal shape. Scale bars, (A) 1 μm and (B) 400 nm. (C) Longitudinal and (D) cross-sectional fracture surfaces of the decalcified FFR showing the honeycomb structure. Scale bars, 400 nm. (E) TEM image of a transverse ultrathin section of the FFR. The yellow arrows indicate the twin boundaries in the nanowires. Not all the boundaries are visible because of the tilting angles. Scale bar, 200 nm. (F) HRTEM image of an aragonite nanowire showing the twin boundary. (Inset) Selected area electron diffraction image of the twin structure revealing that the twin boundary is the (110) plane. Scale bars,

5 nm and (inset) 2 nm⁻¹. (G) TEM and (H) HRTEM images of an ultrathin longitudinal section of the FFR. The aragonite crystals grow along the (002) direction. Scale bars, (G) 200 nm and (H) 3 nm. (I) Morphological orientation of nanowires in the FFR (indicated with the white fan shape). The images in the region were obtained by means of fast Fourier transform (FFT) of the scanning electron microscopy (SEM) images (for example, the FFT image in the box is transformed from the SEM image in the dashed box). Scale bar, 1 μm . (J) Crystallographic orientation (002) (black lines) of the aragonite nanowires in the FFR, which is acquired from the crystal diffractogram. The color of each square indicates the deflection angle of (002) orientation against the mirror plane of the FFR.

Because the morphological and crystallographic orientations of these ordered nanowires are the same, the internal stress in the FFR can be deduced from the stress-induced lattice distortion of the aragonite crystals (33). We therefore investigated the stress states of some microdomains in the FFR by means of high-resolution synchrotron x-ray diffraction. The cell parameter c of the aragonite nanowires at the closed state decreases compared with that at the open state (Fig. 4A and fig. S18), whereas the changes of parameters a and b are much smaller. Because the nanowires grow along the (002) direction, the result indicates that each aragonite nanowire experiences a

large radial load along the longitudinal direction. However, although the FFR endures a larger deformation in the circumferential direction, its elastic modulus along this direction is smaller, and it is the organic matrix that bears most of the deformation (fig. S17). This explains the much smaller changes of a and b as well as the small circumferential loads on the nanowires. The result is thus in good agreement with the properties of the RVE.

The ROAC motions can be implemented hundreds of thousands of times during the course of the shell's lifetime, and thus the FFR that exerts distinct functionalities in different directions also has to be fatigue resistant (Fig. 1C and

fig. S4). Because the aragonite nanowires are extremely long and brittle (34), they should have broken off easily as the FFR undergoes the radial load from the OL. In this respect, the organic matrix, which is resistant to fracture and wraps around each nanowire, can prevent the fragile nanowire from bending and breaking (fig. S19). We evaluated the stress states of the nanowires during the ROAC motions to see how the nanowires can sustain the motions. Because the FFR bears a circumferential deformation, lateral compressive stress or tensile stress should thus be applied to the nanowires.

Atomic-force microscopy (AFM) observation of the FFR fracture surface in liquid reveals,

Fig. 4. In situ stress state analyses of the nano-wires. (A) High-resolution synchrotron x-ray diffraction analysis of the lattice constant variation (from open to closed) of the aragonite crystals. (B) AFM images obtained at “up,” “middle,” and “down” positions in the FFR (fig. S22B) at the open and closed states of the valves. Scale bars, 500 nm. (C) Shift of relative position (Δd) of two adjacent nanowires.

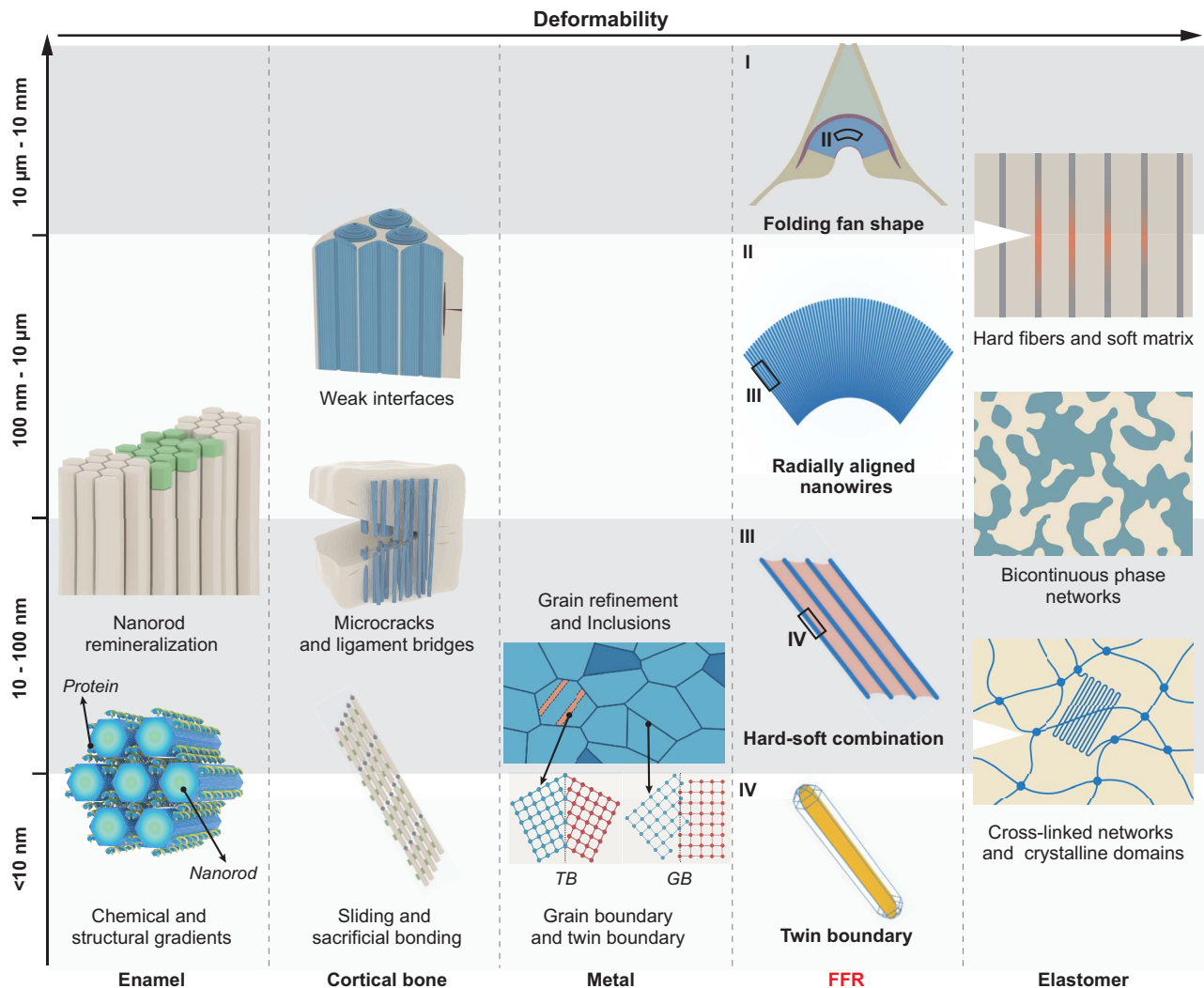
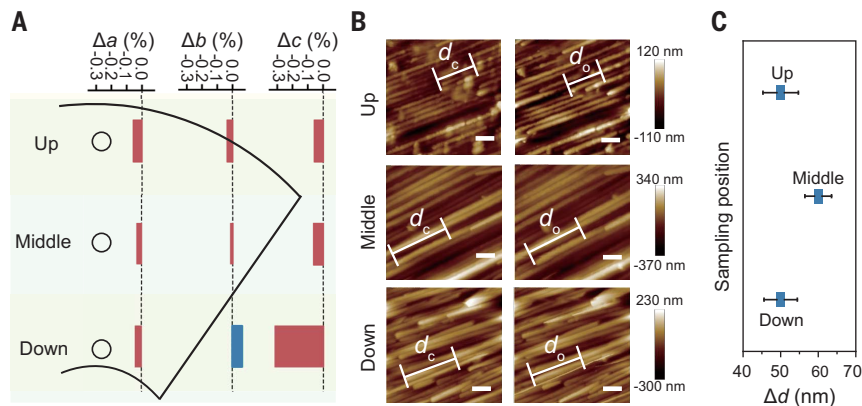


Fig. 5. Antifatigue design of typical biological and artificial structural materials. The antifatigue performance of the structural materials with diverse stiffness relies on their specific structures. Enamel: Chemical and structural gradients inhibit the fatigue crack initiation and propagation; damages can be repaired by the hydroxyapatite nanorod remineralization (10, 39). Cortical bone: Sacrificial bond rupture and collagen fibril sliding impede the crack initiation; microcrack, ligament bridges, and weak interface induce the crack deflection and slows the crack propagation; remodeling substitutes old or damaged bone with new bone tissue (9, 40). Metal: Twin boundaries (TB) and grain boundaries (GB) suppress dislocation activities; nano inclusions retard microcrack propagation (41).

FFR: External load is translated by the folding fan-like structure (I) to circumferential deformation without inducing stress concentration; the hard-soft complex structure consisting of radially aligned nanowires (II) deforms compatibly to sustain the circumferential deformation, while the soft matrix (III) undertakes most of the volume compression; twin boundaries (IV) along the length direction of the nanowires provide a bottom-level guarantee to the aragonite nanowires against bending fracture. Elastomer: Cross-linked networks and crystalline domains raise the threshold of energy release rate; bicontinuous phase networks and a hard fiber and soft matrix complex enhance the crack deceleration and blunting (42).

through comparison of the relative positions of adjacent nanowires, the nanowires' axial sliding indicating a shear force around the nanowires as well as the lateral stresses (Fig. 4, B and C, and fig. S20) (35). We thus simulated the three stress states—compression, tension, and shear—in a two-dimensional numerical model (fig. S21). The FEA results suggest that it is the matrix that bears most of the compressive and shear strains in all the states; no stress concentration is found in the nanowires or the organic matrix. Therefore, the deformation compatibility of this hard-soft complex structure can effectively reduce the possibility of brittle rupture of the aragonite nanowires, by which the fatigue damage of the FFR can be suppressed.

Aragonite belongs to the *Pmcn* space group in which (110) twinning planes can easily develop in aragonite crystals. This makes these orthorhombic crystals exhibit a pseudo-hexagonal appearance (Fig. 3, B and E) (36). As the aragonite nanowires in the FFR grow along the (002) direction, abundant twin boundaries are found in parallel with the axial direction of the nanowires (Fig. 3, E and F). Such twin boundaries can improve the nanowire resistance to bending fracture (37, 38). Therefore, in addition to the higher stress transfer capability of the (002) orientation of the aragonite nanowires, this orientation is also associated with the nanotwin boundary formation that plays a key role in preventing the fracture of the nanowires under cyclic stress states.

Conclusions and outlook

We have revealed the hierarchical structure design of the FFR in the hinge of *C. plicata*, which spans from the macroscale level down to the lattice level. This design is not a simple accumulation of isolated antifatigue mechanisms; rather, each aspect works synergistically (Fig. 5). The notable deformability and load translation capability of the FFR originate from the hierarchical structures, which cannot be achieved by any specific mechanism that acts at only a few length scales. The combination of the functionality and fatigue resistance of the FFR exemplifies how the service life of a material can be prolonged by exploiting the intrinsic properties of each component. Furthermore, *C. plicata* shell also exploits the

inherent crystallographic characteristics of aragonite for the biomineralization of the FFR; this tactic is rarely used in the fabrication of artificial structural materials. Although there is much to learn from this biomineral, we fabricated a proof-of-concept glass-polymer composite with the FFR-like microstructure as a primitive demonstration (fig. S22). The composite exhibits anisotropic mechanical behaviors and good fatigue resistance similar to those of the FFR (supplementary text 2). This biomineral provides a multiscale model for designing structural materials that contain brittle components, such as ceramics, yet require both deformability and fatigue resistance.

REFERENCES AND NOTES

- D. Gu et al., *Science* **372**, eabg1487 (2021).
- S. Bhuniratan et al., *Sci. Transl. Med.* **8**, 343ra83 (2016).
- S. Park, H. Park, S. Seong, Y. Chung, *Sci. Rep.* **10**, 7660 (2020).
- K. J. Miller, *Mater. Sci. Technol.* **9**, 453–462 (1993).
- C. E. Renshaw, E. M. Schulson, *Nature* **412**, 897–900 (2001).
- J. Schijve, *Int. J. Fatigue* **25**, 679–702 (2003).
- J. J. Kruzic, *Science* **325**, 156–158 (2009).
- Y. Shao, H.-P. Zhao, X.-Q. Feng, H. Gao, *J. Mech. Phys. Solids* **60**, 1400–1419 (2012).
- M. E. Launey, M. J. Buehler, R. O. Ritchie, *Annu. Rev. Mater. Res.* **40**, 25–53 (2010).
- D. Bajaj, A. Nazari, N. Eidelman, D. D. Arola, *Biomaterials* **29**, 4847–4854 (2008).
- R. O. Ritchie, *Nat. Mater.* **10**, 817–822 (2011).
- Z. Ma et al., *Sci. Rep.* **6**, 22156 (2016).
- T. Magrini et al., *Nat. Commun.* **10**, 2794 (2019).
- M. J. Kim et al., *Sci. Adv.* **7**, eabg8169 (2021).
- C. Xu, Y. Song, M. Han, H. Zhang, *Microsyst. Nanoeng.* **7**, 25 (2021).
- E. H. Cho et al., *Nanoscale* **10**, 628–638 (2018).
- G. Zan et al., *Matter* **4**, 3232–3247 (2021).
- E. Savazzi, Y. A. O. Peiji, *Lethaia* **25**, 195–209 (1992).
- S. A. Wainwright, *Nature* **224**, 777–779 (1969).
- K. Ono, Y. Kikuch, K. Higashi, N. Tamiya, N. Yasuoka, *J. Biomech.* **23**, 307–312 (1990).
- A. Fernández-Canteli, S. Blasón, B. Pyttel, M. Muniz-Calvente, E. Castillo, *Int. J. Fract.* **223**, 189–196 (2020).
- J. C. Weaver et al., *Science* **336**, 1275–1280 (2012).
- D. Labonte, A.-K. Lenz, M. L. Oyen, *Acta Biomater.* **57**, 373–383 (2017).
- G. Bevelander, H. Nakahara, *Calcif. Tissue Res.* **4**, 101–102 (1969).
- C. Ituarte, D. G. Zelaya, *J. Molluscan Stud.* **81**, 455–465 (2015).
- M. E. Marsh, R. L. Sass, *Science* **208**, 1262–1263 (1980).
- C. Picart, D. E. Discher, *Nature* **448**, 879–880 (2007).
- O. Paris, *Biointerphases* **3**, FB16 (2008).
- A. G. Checa, T. Okamoto, J. Ramirez, *Proc. Biol. Sci.* **273**, 1329–1337 (2006).
- V. Schoeppler et al., *Proc. Natl. Acad. Sci. U.S.A.* **116**, 20388–20397 (2019).
- P. U. P. A. Gilbert et al., *J. Am. Chem. Soc.* **130**, 17519–17527 (2008).
- F. Nudelman, *Semin. Cell Dev. Biol.* **46**, 2–10 (2015).
- B. Pokroy, J. P. Quintana, E. N. Caspi, A. Berner, E. Zolotoyabko, *Nat. Mater.* **3**, 900–902 (2004).
- Z. Wu, Y.-W. Zhang, M. H. Jhon, H. Gao, D. J. Srolovitz, *Nano Lett.* **12**, 910–914 (2012).
- M. Frey et al., *Adv. Sci. (Weinh.)* **6**, 1802190 (2019).

- W. L. Bragg, *Proc. R. Soc. A Contain. Pap. Math. Phys. Character* **105**, 16–39 (1924).
- A. J. Cao, Y. G. Wei, S. X. Mao, *JOM* **60**, 85–88 (2008).
- Y. Tian et al., *Nature* **493**, 385–388 (2013).
- K. A. DeRocher et al., *Nature* **583**, 66–71 (2020).
- J. Li, H. Gong, *Acta Mech. Sin.* **37**, 516–526 (2020).
- D. Rozumek, *Metals (Basel)* **11**, 1957 (2021).
- Y. Huang et al., *Soft Matter* **18**, 5153–5165 (2022).
- S.-H. Yu et al., Deformable hard tissue with high fatigue resistance in the hinge of bivalve *Cristaria plicata*. *Dryad* (2023); <https://doi.org/10.5061/dryad.69p8cz95j>.

ACKNOWLEDGMENTS

The authors thank P. Fratzl from Max Planck Institute for helpful comments and discussions on this work and the manuscript. The authors also thank Z.-L. Zhu for providing micro x-ray diffraction mapping; Y.-G. Gu for fatigue tests; J. Tian and S.-Q. Fu for providing scanning electron microscopy tests and element mapping; T.-W. Li and Y.-R. Wang for providing high-resolution transmission electron microscopy analyses; Z. He, S.-C. Zhang, and J. Pang for AFM tests; Y.-T. Wei (Bruker) and J.-P. Wang (Bruker) for supporting nanoindentation tests; G.-Y. Gao for powder x-ray diffraction tests; W. Wen for high-resolution x-ray diffraction tests; and B.-H. Zhan and R.-D. Wang (Beijing Institute of Fashion Technology) and C.-X. Yu (Anhui University) for their assistance in visualizing this work. This research used Beamline BL14W of the Shanghai Synchrotron Radiation Facility (SSRF) for high-resolution synchrotron x-ray diffraction tests. The authors also thank Shiyanjia Lab (www.shiyanjia.com) for hematoxylin and eosin staining. This work was partially carried out at the USTC Center for Micro and Nanoscale Research and Fabrication.

Funding: This work was supported by financial support from the National Key Research and Development Program of China (grants 2021YFA0715700 and 2018YFE0202201) and the National Natural Science Foundation of China (grants 21701161, 22293044, 12232016, and 12172346). Y.-B.Z. acknowledges funding support from the Youth Innovation Promotion Association CAS (2022465). This work has been supported by New Cornerstone Science Foundation. **Author contributions:** S.-H.Y. and L.-B.M. conceived the idea and designed the experiments. S.-H.Y., L.-B.M., X.-S.M., L.-C.Z., and L.L. wrote and edited the paper. X.-S.M., Y.-F.M., B.Y., and Q.-Z.R. performed the experiments and analyzed the data. L.-C.Z., Y.-B.Z., and H.-A.W. performed theoretical analyses. Y.-B.Z. and D.-C.Z. provided valuable advice for mechanical analyses. Y.-B.Z. and L.-B.M. contributed to antifatigue mechanisms. All authors discussed the results. **Competing interests:** All authors declare that they have no competing interests. **Data and materials availability:** Data are available in the manuscript or the supplementary materials or are deposited in Dryad (43). **License information:** Copyright © 2023 the authors, some rights reserved; exclusive licensee American Association for the Advancement of Science. No claim to original US government works. <https://www.science.org/about/science-licenses-journal-article-reuse>

SUPPLEMENTARY MATERIALS

science.org/doi/10.1126/science.ade2038

Materials and Methods

Supplementary Text

Figs. S1 to S23

Tables S1 to S3

References (44–53)

MDAR Reproducibility Checklist

Movies S1 to S5

Submitted 1 August 2022; accepted 25 April 2023
10.1126/science.ade2038